

JGR Space Physics

RESEARCH ARTICLE

10.1029/2023JA031707

Key Points:

- We developed a numerical model of the energy spectrum of photoelectrons and Auger electrons emitted from the sunlit lunar surface
- The model successfully reproduces Acceleration, Reconnection, Turbulence, and Electrodynamics of the Moon's Interaction with the Sun observations of upward-traveling electrons from the sunlit lunar surface
- The data-model comparison suggests that the emitted electrons can be used as a new tool to remotely infer the lunar surface potential

Correspondence to:

M. Kato,
katomasa@kugi.kyoto-u.ac.jp






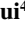


Citation:

Kato, M., Harada, Y., Xu, S., Poppe, A. R., Halekas, J. S., Miyake, Y., et al. (2023). Modeling photoelectron and Auger electron emission from the sunlit lunar surface: A comparison with ARTEMIS observations. *Journal of Geophysical Research: Space Physics*, 128, e2023JA031707. <https://doi.org/10.1029/2023JA031707>

Received 23 MAY 2023

Accepted 17 SEP 2023

Modeling Photoelectron and Auger Electron Emission From the Sunlit Lunar Surface: A Comparison With ARTEMIS Observations

Masahisa Kato¹ , Yuki Harada¹ , Shaosui Xu² , Andrew R. Poppe² , Jasper S. Halekas³ , Yohei Miyake⁴ , Hideyuki Usui⁴ , Masaki N. Nishino⁵ , and Toru Matsumoto⁶

¹Department of Geophysics, Graduate School of Science, Kyoto University, Kyoto, Japan, ²Space Sciences Laboratory, University of California, Berkeley, CA, USA, ³Department of Physics and Astronomy, University of Iowa, Iowa City, IA, USA, ⁴Education Center on Computational Science and Engineering, Kobe University, Kobe, Japan, ⁵Institute of Space and Astronautical Science, Japan Aerospace Exploration Agency, Sagami-hara, Japan, ⁶The Hakubi Center for Advanced Research, Kyoto University, Kyoto, Japan

Abstract Due to the lack of a dense atmosphere, the Moon directly interacts with ambient plasmas and solar radiation, leading to lunar surface charging. Solar X-rays drive the emission of photoelectrons and Auger electrons from the lunar surface to space. The Auger electrons have characteristic energies intrinsic to the photo-emitting atoms and were recently identified at the Moon by Acceleration, Reconnection, Turbulence, and Electrodynamics of the Moon's Interaction with the Sun (ARTEMIS) observations. In this study, we developed a numerical model of the energy spectrum of lunar photoelectrons and Auger electrons, thereby comparing the predicted and observed energy spectra. By adjusting a scaling factor, the model well reproduces the ARTEMIS observations obtained in the solar wind, where the energy spectra are minimally affected by surface charging. Meanwhile, the energy spectra obtained in the geomagnetic tail can be significantly altered by lunar surface potentials. We show that it is difficult to determine a unique combination of the scaling factor and the lunar surface potential with the ARTEMIS energy resolution because of a strong parameter degeneracy. Nevertheless, for a fixed scaling factor, a strong correlation is identified between the lunar surface potentials inferred from the shifts of the energy spectra and those from the upward photoelectron beam energies, providing a proof of concept for the use of the photo-emitted electrons as a new remote sensing tool of the lunar surface potential. We advocate for future observations of lunar electrons with a high energy resolution.

1. Introduction

Since the Moon has no dense atmosphere, the lunar surface is exposed to the ambient plasma. On the sunlit side of the Moon, photoelectrons are emitted from the surface by solar irradiation. The transfer of charge between the lunar surface and space corresponds to electric currents into and out of the surface, and the imbalance of these currents causes surface charging (Whipple, 1981).

Lunar surface charging has been investigated by charged particle measurements on the lunar surface (Freeman & Ibrahim, 1975) and from orbit (Halekas et al., 2008). Lunar Prospector characterized negative lunar surface potentials by electron reflectometry, which was originally utilized to measure the lunar crustal magnetic fields (Lin et al., 1988; Mitchell et al., 2008) and was subsequently applied to probing the electrostatic environment based on energy-dependent loss cones of electrostatically reflected electrons (Halekas et al., 2002). Meanwhile, ion reflectometry was applied to Acceleration, Reconnection, Turbulence, and Electrodynamics of the Moon's Interaction with the Sun (ARTEMIS) data, thereby inferring positive lunar surface potentials (Harada et al., 2017). Another observable signature relevant to lunar surface charging is field-aligned beams of upward electrons that are emitted from the surface and subsequently accelerated by downward electric fields above the negatively charged lunar surface (Halekas et al., 2002). The upward electron beams were observed not only on the lunar night side, where negative surface potentials are naturally expected from the lack of photoemission, but also on the lunar day side in specific environments such as the geomagnetic tail (Halekas et al., 2005), where a simple current balance predicts positive surface potentials.

These dayside negative surface potentials are interpreted in terms of a non-monotonic potential distribution with a potential minimum formed above the lunar surface (Guernsey & Fu, 1970). Based on a comparison of ARTEMIS

observations and particle-in-cell simulations, Poppe et al. (2012) demonstrated that the observed electron beams can be explained by non-monotonic potentials. The presence of non-monotonic potentials is also inferred from ion observations by the Apollo 14 Suprathermal Ion Detector Experiment on the lunar dayside surface (Collier et al., 2017).

In addition to primary photoelectrons directly expelled by solar photons, Auger electrons are emitted from surface materials if the incident photons are sufficiently energetic (Auger, 1925). The Auger electron emission process (Auger process) consists of three electron transition processes. The first process is photoemission from an inner electron shell of an atom, by which a vacancy is generated (called the primary vacancy). In the second process, another electron in an outer electron shell moves to the primary vacancy, producing a photon whose energy is equal to the photon from the second electron transition. In the third process, the photon from the second electron transition causes another electron emission from an outer electron shell. The emitted electron in the final step is called an Auger electron. For explicit distinction of Auger electrons from different electron shells, the Auger electrons are specifically called “XYZ Auger electrons,” where X, Y, and Z refer to the electron shells related to the first, second, and third Auger processes, respectively.

The Auger process has been widely used for Auger Electron Spectroscopy (AES), which analyzes the chemical composition of sample materials at a few nm depths from the surface (e.g., Chang, 1971; Harris, 1968). Lin and Gopalan (1991) proposed that the surface composition of an airless body can be mapped by AES with high-energy resolution electron measurements from lunar orbiters, though lunar Auger electrons were not observationally identified at that time. Decades later, observations of lunar Auger electrons by ARTEMIS were first reported by Xu et al. (2021).

Motivated by the ARTEMIS observations of lunar Auger electrons, we develop a numerical model of the energy spectrum of photoelectrons and Auger electrons emitted from the sunlit lunar surface, which can be directly compared to the observations. The lunar Auger electron observations have a practical implication for the investigation of lunar surface charging. As the Auger electrons are emitted with fixed characteristic energies from the surface, we can infer the electrostatic potential difference between the lunar surface and the spacecraft from the energy shift of the measured Auger electrons from the emitted (known) energies. We explore the feasibility of this concept by analyzing ARTEMIS data obtained in the terrestrial magnetotail, where large variations of the lunar surface potential are observed. The organization of this paper is as follows. Section 2 gives an overview of an example of observations of lunar Auger electrons by ARTEMIS. In Section 3, we describe our energy spectrum model. Section 4 presents comparisons of the model predictions with ARTEMIS observations, and Section 5 summarizes key conclusions.

2. ARTEMIS Observations

In this section, we briefly introduce one of the Auger electron observations reported by Xu et al. (2021). Figure 1 shows a case of Auger electron observations in the solar wind. During the time interval indicated by the two vertical times, a peak near 500 eV can be seen in the upward electron energy spectra with 0° – 22.5° pitch angles (Figures 1a and 1g) obtained on field lines connected to the dayside lunar surface (Figures 1e and 1i) when the Moon was located in the solar wind (Figure 1h). The ~ 500 eV peak is not present in the downward electron energy spectra (Figure 1c). The pitch angle distributions suggest relatively large loss cones during this time interval (Figures 1c and 1d), suggesting a surface origin of the field-aligned electrons. The ~ 500 eV electrons were interpreted as Auger electrons from oxygen atoms of the lunar surface materials. For comparison of these ARTEMIS observations with our model, we focus on an energy range of 100–800 eV because (a) secondary electrons, which are not included in our model, are expected to dominate at low energies ($< \sim 50$ eV) and (b) signals are typically too small above 800 eV in cases of Auger electron observations.

3. Model Description

The basic concept of our energy spectrum model of photoelectrons and Auger electrons is based on Lin and Gopalan (1991) (hereafter LG91), who presented a simple forward model computing photoelectron and Auger electron spectra from an input solar spectrum. As we demonstrate in Section 4, the LG91 model turned out to be too simplified to reproduce the ARTEMIS observations and we made several improvements to the initial LG91-based model by considering more realistic processes such as inelastic collisions, energy dependence of the

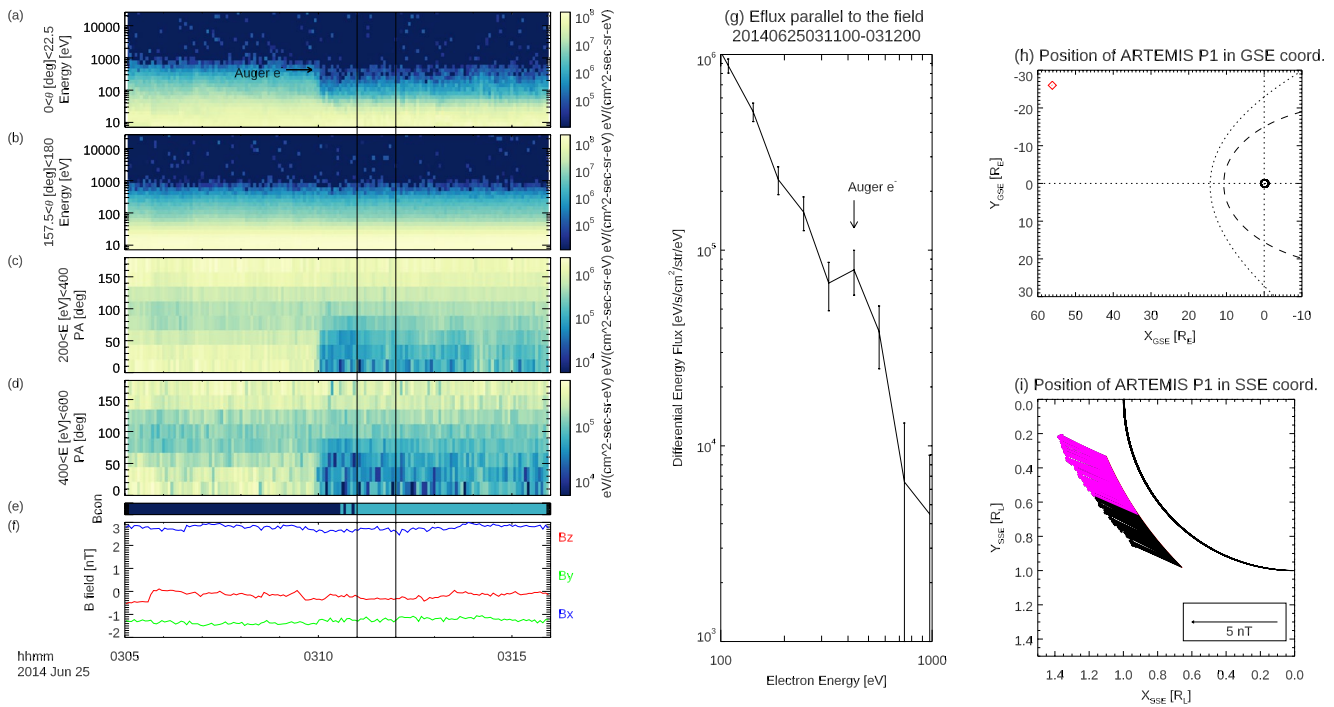


Figure 1. The Auger electron observation in the solar wind region on 25 June 2014 reported by Xu et al. (2021). Energy spectra of electrons with (a) $0^\circ < \theta < 22.5^\circ$, where θ indicates the pitch angle of the electrons, in units of Differential Energy Flux (DEF) and (b) with $157.5^\circ < \theta < 180^\circ$, pitch angle distributions of electrons with (c) $200 < E < 400$ eV, (d) $400 < E < 600$ eV, (e) estimated magnetic field line connection to the Moon (light blue = connected, dark blue = unconnected), (f) magnetic fields in selenocentric solar ecliptic (SSE) coordinates, (g) energy spectrum averaged over the time range indicated by the vertical lines on panels (a–f), and positions of ARTEMIS P1 in (h) geocentric solar ecliptic (GSE), and (i) SSE coordinates. The error bars on panel (g) indicate measurement uncertainties from the counting statistics. The observed magnetic field vectors are projected on panel (i) with magenta and black arrows denoting connected and unconnected field lines, respectively. The dashed line and dotted curved line on panel (h) indicate magnetopause location and bowshock location respectively based on Fairfield (1971). The spacecraft potential U_{SC} at this time is ~ 5 eV.

Inelastic Mean Free Path (IMFP), multiple Auger peaks, and escape efficiency of electrons. Our model calculates the energy spectrum of photoelectrons and Auger electrons emitted from the lunar surface in the following manner.

When a photon with energy ϵ strikes an x th electron shell of atom i (atom number Z_i), the differential flux of photoelectrons f_{pix} , emitted from the lunar surface with energy E can be expressed as

$$f_{pix}(E) dE = \int_{\epsilon} J(\epsilon) \sigma(\epsilon, Z_i, x) \rho_i l(E) \alpha P_p(E, E_p) d\epsilon dE, \quad (1)$$

where $J(\epsilon)$ is the solar irradiation flux of photons at photon energy ϵ , $\sigma(\epsilon, Z_i, x)$ is the photoionization cross-section of the x th electron shell of atom i , ρ_i is the number density of atom i in the surface material, $l(E)$ is the IMFP of electrons with energy E , α is the escape efficiency of photoelectrons due to the surface roughness, $P_p(E, E_p)$ is the probability distribution of the ejected photoelectrons at energy E and for primary photoelectron energy E_p , which includes the effects from elastic and inelastic collisions, and W is the work function of the lunar surface material. In Equation 1, we introduce parameters α , and P in addition to the LG91 formula to include more realistic processes. We use the work function $W = 5$ eV from Feuerbacher et al. (1972). The energy of the primary photoelectrons E_p is determined by the injecting photon energy ϵ , the binding energy of atoms, and the work function as

$$E_p = \epsilon - E_b(Z_i, x) - W, \quad (2)$$

where E_b is the binding energy of x th electron shell of atom i with respect to the Fermi level.

The differential flux of Auger electrons for a specific transition can be expressed as

$$f_{A_{im}}(E) dE = \int_{\epsilon} J(\epsilon) \sigma(\epsilon, Z_i, x_{m1}) \rho_i l(E) \alpha \beta_i P_{A_{im}}(E, E_{A_{im}}) d\epsilon dE, \quad (3)$$

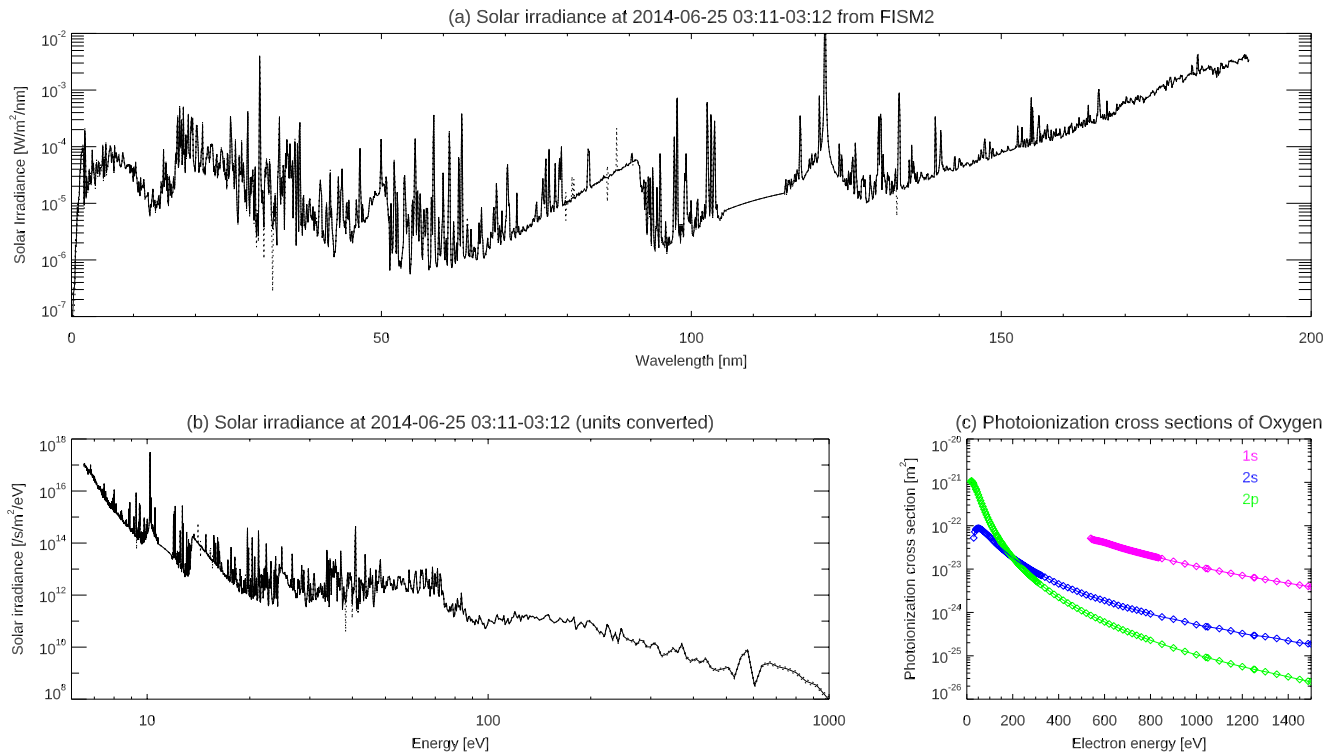


Figure 2. Examples of model inputs, such as Solar irradiance obtained from FISM2 (Chamberlin et al., 2020) in 1 nm wavelength resolution (a), converted and redistributed photon flux (b), and photoionization cross sections of oxygen (Yeh, 1993; Yeh & Lindau, 1985 (<https://vuo.elettra.eu/services/elements/WebElements.html>)). The dashed lines in panels (a and b) indicate the uncertainty of solar irradiance. In panel (c), the magenta, blue, and green lines indicate the cross sections of 1s, 2s, and 2p orbit, respectively.

where J , σ , ρ , l , α , P , and W are the same as those in Equation 1, $E_{A_{im}}$ is the peak energy of Auger electrons through m Auger processes (e.g., $m = \text{KLL, LMM}$) from atom i , β_i is Auger yield, and x_{m_1} is an electron shell related to 1st Auger process (e.g., for KL_1L_{23} Auger process, $x_{m_1} = \text{K}$). $E_{A_{im}}$ is determined as

$$E_{A_{im}} = E_b(Z_i, x_{m_1}) - E_b(Z_i, x_{m_2}) - E_b(Z_i, x_{m_3}) - W, \quad (4)$$

where x_{m_n} ($n = 1, 2, 3$) are electron shells related to n th Auger process. In this study, $E_{A_{im}}$ is calculated from binding energy data from Moulder et al. (1992) and the work function W (Feuerbacher et al., 1972). We calculate the model spectrum in 1 eV resolution. We will explain each variable in Section 3.1.

3.1. Model Inputs

For the solar photon flux J , we utilize a widely used empirical model, FISM2 (Chamberlin et al., 2020). FISM2 provides the solar irradiation flux every 1 nm wavelength (Figure 2a). When we input FISM2 data into our model, we convert wavelength in nm to energy in eV, convert units of the photon flux from $\text{W}/\text{m}^2/\text{nm}$ to $\text{l}/\text{s}/\text{m}^2/\text{eV}$, and redistribute the photon flux into 1 eV resolution bins (Figure 2b).

The photoionization cross-sections, $\sigma(\epsilon, Z_i, x)$, are taken from Yeh and Lindau (1985) and Yeh (1993) (<https://vuo.elettra.eu/services/elements/WebElements.html>). We interpolate the cross-section data to the 1-eV resolution (Figure 2c).

We assume that the lunar surface is composed of atoms of 6 elements (O, Si, Al, Fe, Mg, and Ca) in the same manner as LG91. The number density ρ_i is derived from the average mass densities d of the highland and mare regions and the chemical compositions in atom% (Turkevich, 1973) as shown in Table 1.

Table 1
Atomic Composition of the Lunar Surface and Mass Density d (Turkevich, 1973)

Atoms	Highland (atomic %) $d = 2.96 \text{ g/cm}^3$	Mare (atomic %) $d = 3.19 \text{ g/cm}^3$
O	61.1 ± 0.9	60.3 ± 0.4
Si	16.3 ± 1.0	16.9 ± 1.0
Al	10.1 ± 0.9	6.5 ± 0.6
Fe	1.8 ± 0.3	4.4 ± 0.7
Mg	4.0 ± 0.8	5.1 ± 1.1
Ca	6.1 ± 0.6	4.7 ± 0.4

$l(E)$ is the IMFP of an electron with energy E within the surface material. As IMFP varies with the electron energy, we utilize an energy-dependent formula of IMFP given by Powell and Jablonski (2000) for the ejected electron energy ($>50 \text{ eV}$). In our model, we use the formula for silicon dioxide,

$$l(E) = (254.4E^{-0.9359} + 0.1197E^{0.7989}) \times 10^{-10}, \quad (5)$$

where E is the energy of electrons in eV and $l(E)$ is in m.

β is the Auger yield, which represents the probabilities of the Auger electron emission in the third step of the Auger processes as opposed to the X-ray fluorescence. Schönfeld and Janßen (1996) indicate that β varies with atomic number as shown in Table 2. Table 2 does not include Si, Al, and Mg because the Auger energy peaks are out of the energy range of 100–1,000 eV.

P_p is the electron energy distribution function for photoemission, which includes the elastic peak of photoelectrons with no energy loss and a low-energy tail of inelastically scattered electrons. P_A is the electron energy distribution function for Auger emission. Depending on the element, P_A can include multiple peaks corresponding to multiple transitions (Table 2), each having the inelastic tail. For the inelastic tail distribution, we adopt the Tougaard (1997) distribution,

$$A(T) = \frac{BT}{(C - T^2)^2 + DT^2}, \quad (6)$$

where B , C , and D are empirically determined parameters for different materials, and T is the energy loss with respect to the elastic peak energy. To approximate inelastic scattering within the lunar regolith materials, we apply $B = 325 \text{ eV}^2$, $C = 542 \text{ eV}^2$, and $D = 275 \text{ eV}^2$ for SiO_2 (Tougaard, 1997). Consequently, the function P_p becomes

$$P_p(E, E_p) = \begin{cases} \delta(E_p - E) + \frac{B(E_p - E)}{[C - (E_p - E)^2]^2 + D(E_p - E)^2} & (E_p - E \geq 0) \\ 0 & (E_p - E < 0) \end{cases}, \quad (7)$$

where E_p is the photoelectron primary energy with no energy loss. $P_{A_{im}}$ becomes

$$P_{A_{im}}(E, E_{A_{im}}) = h_{im} p_{im}(E, E_{A_{im}}), \quad (8)$$

where

$$p_{im}(E, E_{A_{im}}) = \begin{cases} \delta(E_{A_{im}} - E) + \frac{B(E_{A_{im}} - E)}{[C - (E_{A_{im}} - E)^2]^2 + D(E_{A_{im}} - E)^2} & (E_{A_{im}} - E \geq 0) \\ 0 & (E_{A_{im}} - E < 0) \end{cases}, \quad (9)$$

Table 2
Auger Transitions and Energies (Moulder et al., 1992) in an Energy Range of 100–1,000 eV, and Auger Yield (Schönfeld & Janßen, 1996) Used in Our Model

Element	Transition	Peak energy (eV)	Normalized peak height h_m	Auger yield β
O	KL ₂₃ L ₂₃	509	0.510	~1.000
	KL ₁ L ₂₃	488	0.283	
	KL ₁ L ₁	474	0.207	
Ca	L ₃ M ₂₃ M ₂₃	290	1.000	0.831
Fe	L ₃ M ₄₅ M ₄₅	703	0.286	0.645
	L ₃ M ₂₃ M ₄₅	648	0.355	
	L ₃ M ₂₃ M ₂₃	599	0.359	

m indicates the Auger process (such as KL₁L₂), and h_m is the normalized peak heights of multiple peaks emitted from the same element of atoms.

α represents the escape efficiency. As opposed to emission from an ideal flat surface, some of the ejected electrons from the lunar surface will be reabsorbed because of the porous lunar regolith. A laboratory experiment by Dove et al. (2018) showed that photoemission currents from a powder surface are reduced by 60%–80% compared to that from a flat solid surface, implying $0.2 \lesssim \alpha \lesssim 0.4$. However, since little knowledge has been obtained for α of the lunar regolith, we treat α as a free parameter and we assume that it is energy independent for simplicity. We note that this scaling factor is the only free parameter in our model.

The errors of input parameters are considered as follows. For the solar photon flux J , the uncertainty of the flux is given by the FISM2 model (Chamberlin

et al., 2020). We converted units of the error as same as the flux and interpolated to 1 eV resolution bins in the same manner as the flux. For the photoionization cross-sections σ , the error is assumed 10% based on the description on page 4 of Yeh and Lindau (1985). For the chemical composition, the variability from the average is given by Turkevich (1973) as shown in Table 1. For IMFP l , Powell and Jablonski (2000) give the uncertainty of the fitting by Equation 5 as 6.73%. Although the error of Auger yield β is not given numerically in the literature, we assume the error of β as 0.02 according to the error bars of Figure 1 in Schönfeld and Janßen (1996). As the accuracy of the electron energy distribution function P is indicated 5%–10% in Tougaard (1997), we assume the error of P in this model is 10%.

The error propagation is calculated as follows. Since the flux is calculated by Equation 1 for the photoelectrons, the error of photoelectron flux for each electron energy and each photon energy $\delta F_p(E, \epsilon_j)$ is calculated by

$$\delta F_p(E, \epsilon_j) = \sqrt{\left(\frac{\partial F_p}{\partial J}\right)^2 (\delta J)^2 + \left(\frac{\partial F_p}{\partial \sigma}\right)^2 (\delta \sigma)^2 + \left(\frac{\partial F_p}{\partial \rho}\right)^2 (\delta \rho)^2 + \left(\frac{\partial F_p}{\partial l}\right)^2 (\delta l)^2 + \left(\frac{\partial F_p}{\partial P}\right)^2 (\delta P)^2}, \quad (10)$$

where δJ , $\delta \sigma$, $\delta \rho$, δl , and δP are uncertainties of J , σ , ρ , l , and P , respectively. The uncertainty of photoelectron flux for each electron energy $\delta f_p(E)$ is calculated by

$$\delta f_p(E) = \sum_j \delta F_p(E, \epsilon_j) \quad (11)$$

The error of Auger electron flux δF_A is similarly calculated from δJ , $\delta \sigma$, $\delta \rho$, δl , δP , and $\delta \beta$, where $\delta \beta$ is the uncertainty of β .

3.2. Prediction of Measured Fluxes From the Model

To compare the model energy spectrum at 1 eV resolution with the ARTEMIS electron measurements, we derive predicted ARTEMIS measurements of electron fluxes by convolving the model spectrum with the instrument energy response. The electron electrostatic analyzer (ESA) onboard ARTEMIS has the analyzer energy resolution $\Delta E/E = 17\%$ and the energy sweep resolution is 32% (McFadden et al., 2008). We reconstruct the energy response of ESA by combining the four sub-energy steps for each of the 31 energy channels, the information on which can be found in a publicly available code, `thm_read_esa_sweep_burst_mode.pro`, included in SPEDAS (Angelopoulos et al., 2019). The error of predicted measurements is calculated by convolving the error of the flux δf with the energy response of ESA.

4. Comparison of the Model With ARTEMIS Observations

4.1. Observations in the Solar Wind

We first show comparisons of the model predictions with ARTEMIS observations in the solar wind. When the Moon is located in the solar wind, both the sunlit lunar surface potential and the spacecraft potential are usually on the order of a few volts positive up to $\sim +10$ V (Freeman & Ibrahim, 1975; Whipple, 1981). Since the expected potential difference between the sunlit lunar surface and the spacecraft is sufficiently small compared to the energy range of our interest, 100–800 eV, we assume no energy shift between the emitted and measured electrons for the observations in the solar wind.

Figure 3a shows an example of the model-data comparison for the event shown in Figure 1. We determine the best-fit parameter α by minimizing the total squared difference of logarithms of the modeled and observed fluxes calculated for every 0.01 in α , $S(\alpha) = \sum (\log F_m(\alpha) - \log F_o)^2$, in the energy range $100 \text{ eV} < E < 800 \text{ eV}$. The model-predicted measurement (magenta) is in good agreement with the ARTEMIS observation (black). Meanwhile, Figure 3b compares the same observation with a model result under the simplified assumptions of LG91.

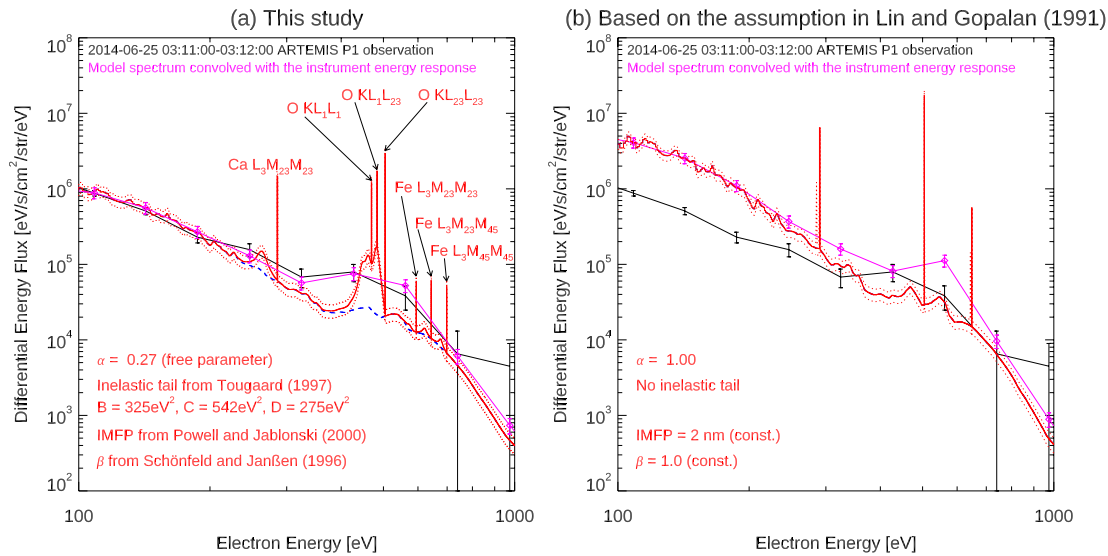


Figure 3. An example of comparisons between the model observed energy spectra with the model spectra (a) derived in this study and (b) based on the simplified assumptions equivalent to Lin and Gopalan (1991). The red lines indicate the differential energy flux calculated by the model in 1 eV energy resolution. The magenta lines show the predicted measurements derived from the model spectra convolved with the instrument response. The black lines indicate the ARTEMIS observations. The blue dashed curve in panel (a) shows the energy spectra without Auger electron emission.

Table 3 summarizes the treatments of the model inputs in this study and LG91. We highlight that the overall spectral slope and the shape of the ~ 500 eV peak are better reproduced in Figure 3a compared to Figure 3b. Specifically, the energy-dependent IMFP changes the overall spectral slope, and the inclusion of the multiple Auger peaks and inelastic low-energy tail modifies the Auger peak shape.

We found similar observations at least 10 events. Here we present two other representative ARTEMIS observations in the solar wind. Figures 4a and 4b show comparisons between the observed energy spectra and the model spectra on 13 January 2013 and 19 June 2022, respectively. In both cases, the model prediction is in general agreement with the ARTEMIS observations, though some variabilities are found in the observed electron spectra.

4.2. Observations in the Terrestrial Magnetotail

As opposed to dayside lunar surface charging in the solar wind, the lunar surface potential is highly variable in the terrestrial magnetotail (Halekas et al., 2008). Since the photoelectrons and Auger electrons are accelerated/decelerated according to the potential difference between the spacecraft and the lunar surface, the resulting energy shift needs to be considered when comparing the model predictions and ARTEMIS observations. As the spacecraft potential is measured by ARTEMIS, the lunar surface potential is an additional free parameter for fitting of the model to the measured electron energy spectra in the geomagnetic tail.

We first present a case study of ARTEMIS observations in the magnetotail lobe region (Figure 5). This event is one of the reported Auger electron events by Xu et al. (2021) and was analyzed by Harada et al. (2017), who derived the lunar surface potential U_M of +15–25 V based on the observed energy-dependent loss cone of electrostatically reflected lobe ions (ion reflectometry). For a non-zero potential difference, we shift the 1-eV resolution model energy spectrum such that the distribution function is conserved, and the shifted spectrum is convolved with the instrument response to derive the model-predicted measurements. We conduct a grid search for the best-fit parameters (α and $U_M = -(S.E. - U_{sc})$, where $S.E.$ is the shifted energy between the lunar surface and the spacecraft and U_{sc} is spacecraft potential observed by ARTEMIS) based on the same metric, $S(\alpha, S.E.) = \sum (\log F_m(\alpha, S.E.) - \log F_o)^2$ calculated for every 0.01 in α and every 1 eV in $S.E.$, as the solar wind case. The error distribution as a function of α and U_M is shown in Figure 6a and the best-fit model and observations are compared in Figure 6b. The best-fit parameters are $(\alpha, U_M) = (0.52, 40 \text{ V})$. This U_M is larger than the

Table 3
Variables in Our Model and Their References, Comparison With Lin and Gopalan (1991) Model

	Variables	Lin and Gopalan (1991) model	Our model
$J(\epsilon)$	Solar irradiation flux	Mewe (1972)	FISM2 Chamberlin et al. (2020)
$\sigma(\epsilon, Z_p, x)$	Photoionization cross section	Scofield (1973)	Yeh and Lindau (1985)
ρ_i	Number density of atom i	Taylor (1975)	Turkevich (1973)
$l(\epsilon)$	IMFP of electrons	Assumed that $l = 2$ nm (constant)	Powell and Jablonski (2000)
α	Escape efficiency of electrons	Assumed that $\alpha = 1$	Determined by model-observation comparison
β	Auger yield	Assumed that $\beta = 1$	Schönfeld and Janßen (1996)
$P_p(\epsilon, E)$	Distribution function of photoelectrons	Delta function	Delta function (elastic) + Tougaard (1997) distribution (inelastic)
$P_A(E_{Ak})$	Distribution function of Auger electrons	Only considered single peak	Considered multiple peaks

ion reflectometry results of +15–25 V. We note that Figure 6a shows a strong parameter degeneracy, resulting in ambiguous determination of α and U_M . This is because increasing α and decreasing U_M have similar effects as demonstrated by the raised overall spectrum with decreasing U_M in Figure 6b. Ideally, electron measurements with a sufficiently high-energy resolution would enable unambiguous determination of U_M by resolving the shift of the distinct Auger peaks. However, the rather coarse energy resolution of ESA mostly smears out the Auger features, hindering the detailed investigation of individual peaks.

The magnetotail lobe case suggests that it is difficult to unambiguously determine α and U_M from the currently available data. Nonetheless, if we can assume that α does not vary significantly over a short segment of ARTEMIS observations, we may be able to infer the degree of U_M variations within the segment.

Figure 7 presents such an exercise with a well-studied event in the plasma sheet reported by Poppe et al. (2012). As shown in Figure 7a, we observe monoenergetic electron beams with varying energies, implying rapid variations of the negative (non-monotonic) potential on the dayside lunar surface. We extract the beam energy (Figure 7c) by fitting a Gaussian to the peak of differential energy flux detected above the spacecraft potential.

During 12:14–12:16 UTC (indicated by the red dashed vertical lines in Figures 7a–7e), a ~ 500 eV peak was observed in the upward electrons (Figure 7a), indicating the presence of Auger electrons. During this time interval, no electron beam was observed (Figure 7a), implying that the magnitude of the negative surface potential is small. Based on these observations, we set $U_M = 0$ and determine the best-fit α for this time interval as shown in Figure 7f. We note that the agreement between the model and the observation is not as good as that in the solar wind case, possibly because of surface-scattered or magnetically scattered hot plasma sheet electrons. Here α might function as an empirical adjusting parameter rather than representing the escaping efficiency as originally defined.

Next, we assume that the determined α is constant during 12:00–12:13 (indicated by the black dashed vertical lines in Figures 7a–7e) and determine the best-fit energy shift (Figure 7d). To eliminate the electron beams with energies up to ~ 200 eV (Figures 7a and 7c) from fitting, we determine the best-fit energy shift based on $S(S.E.) = \sum (\log F_m(S.E.) - \log F_o)^2$ in an energy range of $200 \text{ eV} < E < 800 \text{ eV}$.

Figure 7g compares the beam energy (Figure 7c) and the best-fit energy shift (Figure 7d). The relationship between these energies and the potential structure is illustrated in Figure 8. The beam energy (red) is determined by the potential minimum, U_{\min} , whereas the energy shift (blue) is determined by the surface potential, U_M . As shown in Figure 7g, we observe a strong correlation between the two. By correcting for the spacecraft potential, we derive the non-monotonic potential minimum from the beam energy and the lunar surface potential from the energy shift (Figure 7h). This result suggests a strong correlation between the non-monotonic potential minimum and the lunar surface potential. The observed correlation is consistent with an expectation that the depth of the potential minimum with respect to the surface potential, $U_M - U_{\min}$, should be determined by the characteristic energy of the emitted photoelectrons and be largely independent of the incident electron variations. Also, PIC simulations predict that the lunar surface potential varies in sync with the potential minimum in response to the ambient plasma variations (Poppe et al., 2011, 2012). The consistent prediction from the simulations suggests that the energy shift of the lunar photoelectrons and Auger electrons could provide valuable information on the lunar surface potential.

5. Conclusions

In this study, we developed the numerical model of the energy spectrum of photoelectrons and Auger electrons emitted from the sunlit lunar surface. The model reproduces the ARTEMIS observations generally well in the solar wind, where the electron measurements are less affected by the potential difference between the lunar surface and the spacecraft. To explore the feasibility of remote measurements of the lunar surface potential with the lunar Auger electrons, we analyzed the two magnetotail cases, in which the lunar surface potential was estimated by different methods. The magnetotail lobe case suggests that an unambiguous

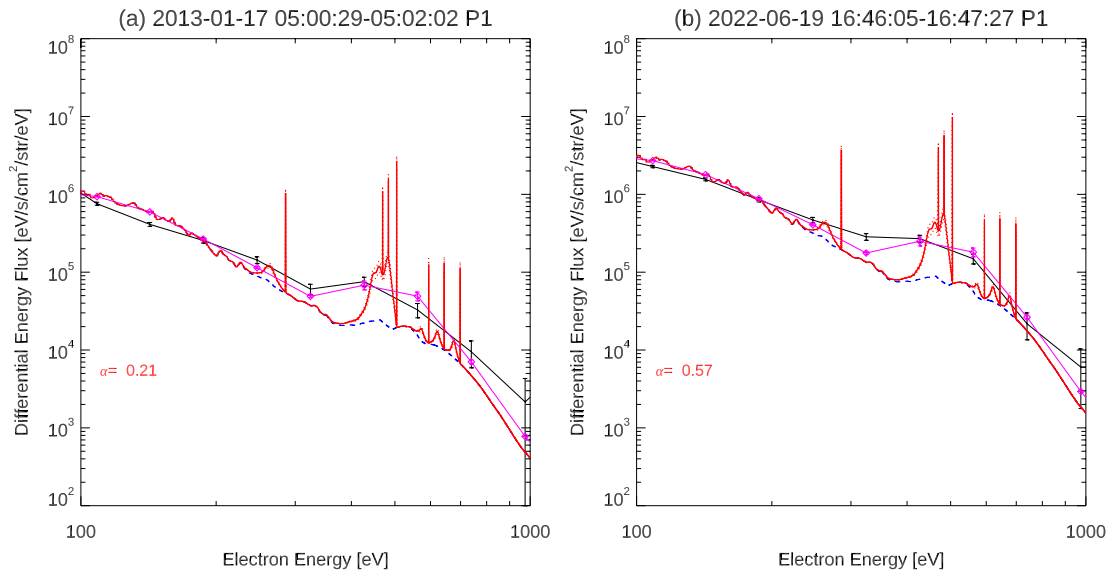


Figure 4. Examples of comparisons between the observed energy spectra and the model spectra (a) on 13 January 2013 and (b) on 19 June 2022 in the same format as Figure 3a.

determination of the lunar surface potential is challenging with the coarse energy resolution of ARTEMIS ESA. The energy shift fitting and beam energy analysis for the plasma sheet case suggest a strong correlation between the lunar surface potential and the non-monotonic potential minimum as predicted by PIC simulations. The results motivate future high-energy resolution measurements of electrons at airless bodies. It is notable that such high-energy resolution electron measurements might also enable Auger Electron Spectroscopy investigation of the surface composition of airless bodies as first envisioned by LG91.

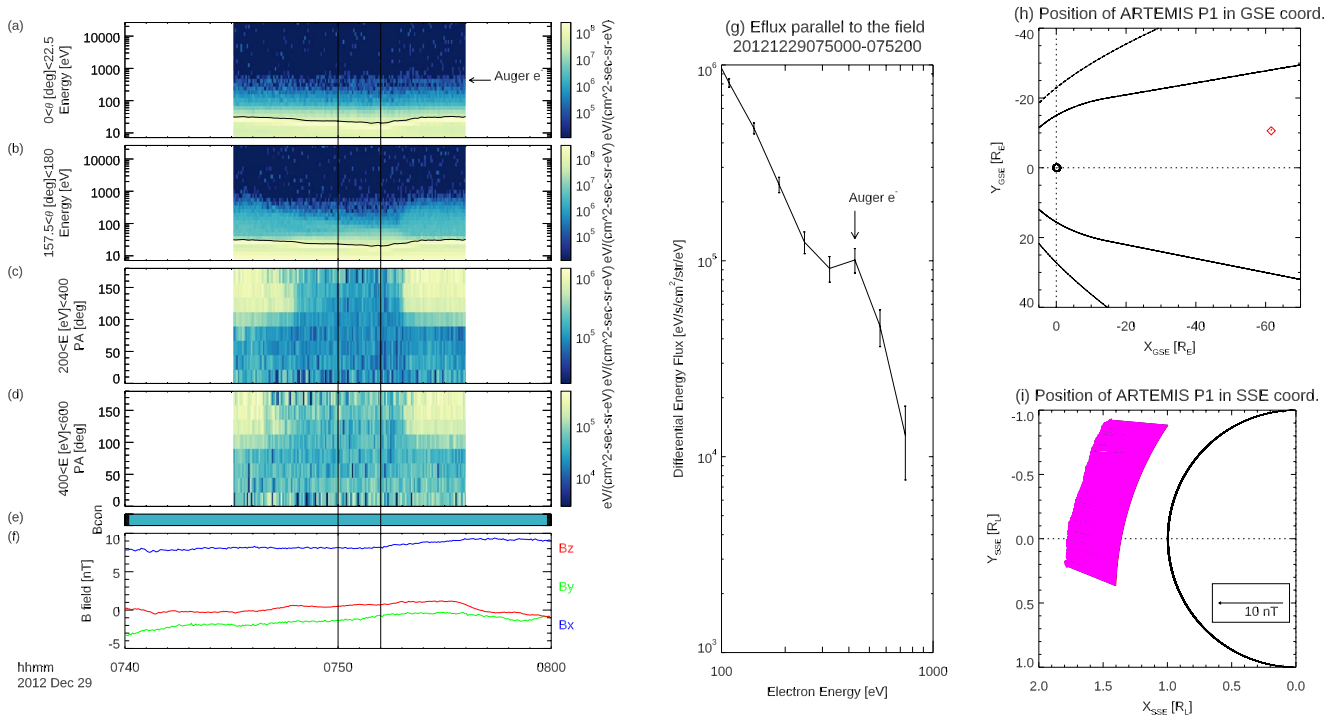


Figure 5. The Auger electron observation in the magnetotail lobe region on 29 December 2012 reported by Xu et al. (2021) in the same format as Figure 1. The black lines in panels (a and b) indicate the observed spacecraft potential.

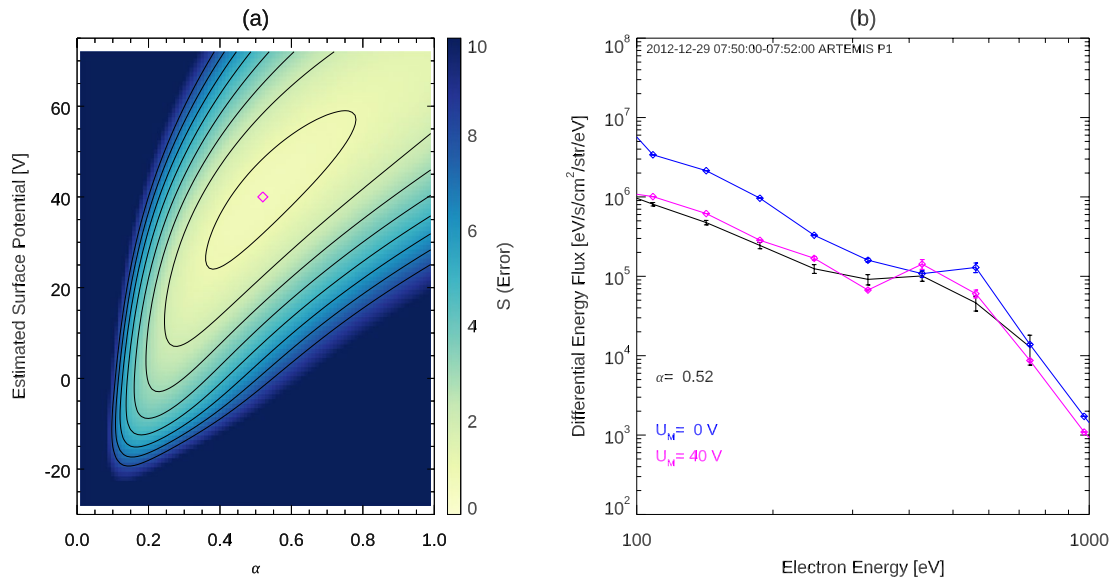


Figure 6. Total error S distribution for the parameter α and the estimated surface potential (a), and an example of the electron energy spectrum calculated by our model assuming deceleration by surface potential (b) on 29 December 2012 event (shown in Figure 5). The magenta diamond on panel (a) indicates best-fit parameters. The black line and error bar in the right figure are similar to Figure 3. The black lines on panel (a) are contour diagrams of $S = \sum (\log F_m - \log F_o)^2$.

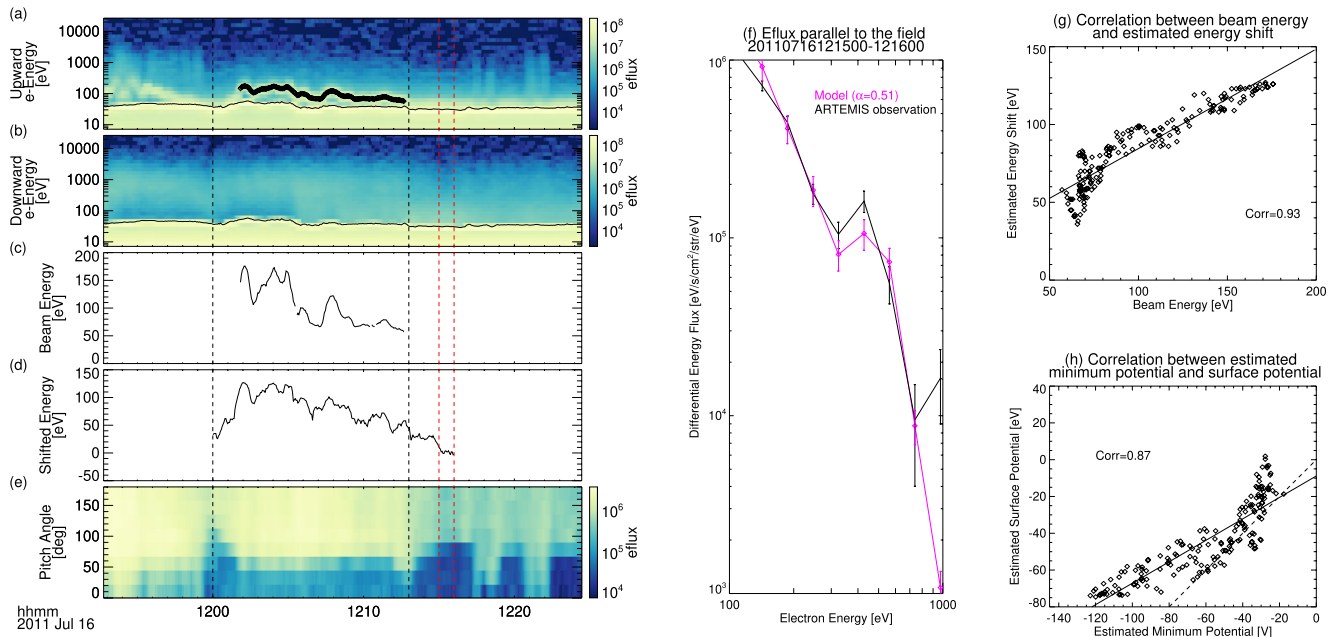


Figure 7. Running-averaged (30 s) energy spectra in units of differential energy flux (DEF) of (a) upward electrons ($0^\circ < \theta < 22.5^\circ$), and (b) downward electrons ($157.5^\circ < \theta < 180^\circ$), (c) upward electron beam energy indicated by the diamonds on panel (a), (d) electron energy shift between the lunar surface and the spacecraft estimated by fitting our model to the data, (e) pitch angle spectra of electrons ($500 \text{ eV} < E < 1,000 \text{ eV}$), (f) energy spectrum averaged over the time range indicated by the red dashed vertical lines on (a–e) (black line with error bars) and model-predicted measurements ($\alpha = 0.51$, magenta line), (g) scatter plot of the beam energy (panel (c)) and the energy shift (panel (d)), and (h) scatter plot of the estimated minimum potential and the estimated surface potential. The black solid lines in panels (a) and (b) indicate the observed spacecraft potential. The black solid lines in panels (g) and (h) indicate the linear fitting results.

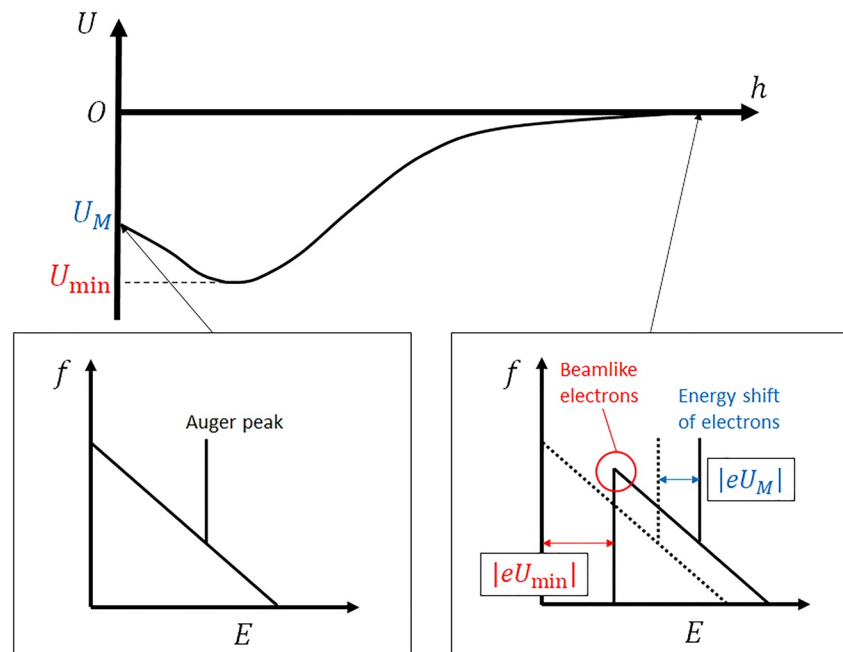


Figure 8. A schematic diagram of the potential distribution above the lunar surface and the electron energy spectra at the lunar surface and above the surface. The red arrow indicates the magnitude of energy of beamlike electrons and the blue arrow indicates the magnitude of the energy shift of electrons.

Data Availability Statement

All ARTEMIS data used in this paper are publicly available at the ARTEMIS sites (<http://themis.ssl.berkeley.edu/data/themis/thb/>; <http://themis.ssl.berkeley.edu/data/themis/thc/>). Data processing was done using SPEDAS (Angelopoulos et al., 2019). The results presented in this document rely on the FISM2 model described in Chamberlin et al. (2020). The FISM2 data were accessed via the LASP Interactive Solar Irradiance Datacenter (LISIRD) (https://lasp.colorado.edu/eve/data_access/eve_data/fism/flare_hr_data/).

Acknowledgments

We acknowledge NASA contract NAS5-02099 and V. Angelopoulos for use of data from the THEMIS Mission. Specifically: C. W. Carlson and J. P. McFadden for use of ESA data and K. H. Glassmeier, U. Auster and W. Baumjohann for the use of FGM data provided under the lead of the Technical University of Braunschweig and with financial support through the German Ministry for Economy and Technology and the German Center for Aviation and Space (DLR) under contract 50 OC 0302. YH is supported by JSPS KAKENHI Grant (22K14085). This work was supported by JST, the establishment of university fellowships towards the creation of science technology innovation, Grant JPMJFS2123. Masahisa Kato is supported by Takenaka Scholarship Foundation. We wish to thank Kumano dormitory community at Kyoto University for their generous financial and living assistance to Masahisa Kato.

References

- Angelopoulos, V., Cruce, P., Drozdov, A., Grimes, E. W., Hatzigeorgiu, N., King, D. A., et al. (2019). The space physics environment data analysis system (SPEDAS). *Space Science Reviews*, 215(1), 9. <https://doi.org/10.1007/s11214-018-0576-4>
- Auger, P. (1925). Sur l'effet photoélectrique composé. *Journal de Physique et le Radium*, 6(6), 205–208. <https://doi.org/10.1051/jphysrad:0192500606020500>
- Chamberlin, P. C., Eparvier, F. G., Knoer, V., Leise, H., Pankratz, A., Snow, M., et al. (2020). The flare irradiance spectral model-version 2 (FISM2). *Space Weather*, 18(12), e2020SW002588. <https://doi.org/10.1029/2020SW002588>
- Chang, C. C. (1971). Auger electron spectroscopy. *Surface Science*, 25(1), 53–79. [https://doi.org/10.1016/0039-6028\(71\)90210-X](https://doi.org/10.1016/0039-6028(71)90210-X)
- Collier, M. R., Newheart, A., Poppe, A. R., Hills, H. K., & Farrell, W. M. (2017). Stair-step particle flux spectra on the lunar surface: Evidence for nonmonotonic potentials? *Geophysical Research Letters*, 44(1), 79–87. <https://doi.org/10.1002/2016GL071457>
- Dove, A., Horányi, M., Robertson, S., & Wang, X. (2018). Laboratory investigation of the effect of surface roughness on photoemission from surfaces in space. *Planetary and Space Science*, 156, 92–95. <https://doi.org/10.1016/j.pss.2017.10.014>
- Fairfield, D. H. (1971). Average and unusual locations of the Earth's magnetopause and bow shock. *Journal of Geophysical Research*, 76(28), 6700–6716. <https://doi.org/10.1029/JA076i028p06700>
- Feuerbacher, B., Anderegg, M., Fitton, B., Laude, L., Willis, R., & Grard, R. (1972). Photoemission from lunar surface fines and the lunar photoelectron sheath. In *Lunar and planetary science conference proceedings* (Vol. 3, p. 2655).
- Freeman, J., & Ibrahim, M. (1975). Lunar electric fields, surface potential and associated plasma sheaths. *The Moon*, 14(1), 103–114. <https://doi.org/10.1007/bf00562976>
- Guernsey, R. L., & Fu, J. H. M. (1970). Potential distribution surrounding a photo-emitting, plate in a dilute plasma. *Journal of Geophysical Research*, 75(16), 3193–3199. <https://doi.org/10.1029/JA075i016p03193>
- Halekas, J. S., Delory, G. T., Lin, R. P., Stubbs, T. J., & Farrell, W. M. (2008). Lunar prospector observations of the electrostatic potential of the lunar surface and its response to incident currents. *Journal of Geophysical Research*, 113(A9), A09102. <https://doi.org/10.1029/2008JA013194>
- Halekas, J. S., Lin, R. P., & Mitchell, D. L. (2005). Large negative lunar surface potentials in sunlight and shadow. *Geophysical Research Letters*, 32(9), L09102. <https://doi.org/10.1029/2005GL022627>
- Halekas, J. S., Mitchell, D. L., Lin, R. P., Hood, L. L., Acuña, M. H., & Binder, A. B. (2002). Evidence for negative charging of the lunar surface in shadow. *Geophysical Research Letters*, 29(10), 77-1–77-4. <https://doi.org/10.1029/2001GL014428>

- Harada, Y., Poppe, A. R., Halekas, J. S., Chamberlin, P. C., & McFadden, J. P. (2017). Photoemission and electrostatic potentials on the dayside lunar surface in the terrestrial magnetotail lobes. *Geophysical Research Letters*, *44*(11), 5276–5282. <https://doi.org/10.1002/2017GL073419>
- Harris, L. A. (1968). Analysis of materials by electron-excited auger electrons. *Journal of Applied Physics*, *39*(3), 1419–1427. <https://doi.org/10.1063/1.1656374>
- Lin, R. P., Anderson, K., & Hood, L. (1988). Lunar surface magnetic field concentrations antipodal to young large impact basins. *Icarus*, *74*(3), 529–541. [https://doi.org/10.1016/0019-1035\(88\)90119-4](https://doi.org/10.1016/0019-1035(88)90119-4)
- Lin, R. P., & Gopalan, R. (1991). Mapping the composition of planetary surfaces by auger electron spectroscopy. *Review of Scientific Instruments*, *62*(3), 660–666. <https://doi.org/10.1063/1.1142064>
- McFadden, J. P., Carlson, C. W., Larson, D., Ludlam, M., Abiad, R., Elliott, B., et al. (2008). The THEMIS ESA plasma instrument and in-flight calibration. *Space Science Reviews*, *141*(1–4), 277–302. <https://doi.org/10.1007/s11214-008-9440-2>
- Mewe, R. (1972). Calculated solar x-radiation from 1 to 60 Å. *Solar Physics*, *22*(2), 459–491. <https://doi.org/10.1007/BF00148711>
- Mitchell, D., Halekas, J., Lin, R., Frey, S., Hood, L., Acuña, M., & Binder, A. (2008). Global mapping of lunar crustal magnetic fields by lunar prospector. *Icarus*, *194*(2), 401–409. <https://doi.org/10.1016/j.icarus.2007.10.027>
- Moulder, J. F., Stickle, W. F., Sobol, E. P., & Bomben, K. D. (1992). *Handbook of x-ray photoelectron spectroscopy*. Perkin-Elmer Corporation Physical Electronics Division.
- Poppe, A. R., Halekas, J. S., Delory, G. T., Farrell, W. M., Angelopoulos, V., McFadden, J. P., et al. (2012). A comparison of ARTEMIS observations and particle-in-cell modeling of the lunar photoelectron sheath in the terrestrial magnetotail. *Geophysical Research Letters*, *39*(1), L01102. <https://doi.org/10.1029/2011GL050321>
- Poppe, A. R., Halekas, J. S., & Horányi, M. (2011). Negative potentials above the day-side lunar surface in the terrestrial plasma sheet: Evidence of non-monotonic potentials. *Geophysical Research Letters*, *38*(2), L02103. <https://doi.org/10.1029/2010GL046119>
- Powell, C. J., & Jablonski, A. (2000). Evaluation of electron inelastic mean free paths for selected elements and compounds. *Surface and Interface Analysis*, *29*(2), 108–114. [https://doi.org/10.1002/\(SICI\)1096-9918\(200002\)29:2<108::AID-SIA700>3.0.CO;2-4](https://doi.org/10.1002/(SICI)1096-9918(200002)29:2<108::AID-SIA700>3.0.CO;2-4)
- Schönfeld, E., & Janßen, H. (1996). Evaluation of atomic shell data. *Nuclear Instruments and Methods in Physics Research Section A: Accelerators, Spectrometers, Detectors and Associated Equipment*, *369*(2), 527–533. [https://doi.org/10.1016/S0168-9002\(96\)80044-1](https://doi.org/10.1016/S0168-9002(96)80044-1)
- Scofield, J. H. (1973). *Theoretical photoionization cross sections from 1 to 1500 kev. (Tech. Rep.)*. California University, Lawrence Livermore Lab.
- Taylor, S. R. (1975). *Lunar science: A post-Apollo view: Scientific results and insights from the lunar samples*. Pergamon Press.
- Tougaard, S. (1997). Universality classes of inelastic electron scattering cross-sections. *Surface and Interface Analysis*, *25*(3), 137–154. [https://doi.org/10.1002/\(SICI\)1096-9918\(199703\)25:3<137::AID-SIA230>3.0.CO;2-L](https://doi.org/10.1002/(SICI)1096-9918(199703)25:3<137::AID-SIA230>3.0.CO;2-L)
- Turkevich, A. (1973). The average chemical composition of the lunar surface. In *Lunar science conference*.
- Whipple, E. C. (1981). Potentials of surfaces in space. *Reports on Progress in Physics*, *44*(11), 1197–1250. <https://doi.org/10.1088/0034-4885/44/11/002>
- Xu, S., Poppe, A. R., Harada, Y., Halekas, J. S., & Chamberlin, P. C. (2021). Lunar photoemission yields inferred from ARTEMIS measurements. *Journal of Geophysical Research: Planets*, *126*(6), e2020JE006790. <https://doi.org/10.1029/2020JE006790>
- Yeh, J. J. (1993). *Atomic calculation of photoionization cross-sections and asymmetry parameters*. Gordon and Breach Science Publishers. Retrieved from <https://vuo.elettra.eu/services/elements/WebElements.html>
- Yeh, J., & Lindau, I. (1985). Atomic subshell photoionization cross sections and asymmetry parameters: $1 \leq z \leq 103$. *Atomic Data and Nuclear Data Tables*, *32*(1), 1–155. [https://doi.org/10.1016/0092-640X\(85\)90016-6](https://doi.org/10.1016/0092-640X(85)90016-6)